Advanced Sustainable Systems

ADVANCED SUSTAINABLE SYSTEMS
www.advsustainsys.com

RESEARCH ARTICLE OPEN ACCESS

A Natural Solvent-Based Gel Electrolyte for Stable and Sustainable Zinc-Ion Batteries

Gokce Komurcuoglu[1] | Sadaf Adhami[2] | Gulsah Yaman Uzunoglu[3,4] | Recep Yuksel[2,4,5]

[1]Department of Chemical Engineering, Eskisehir Osmangazi University (ESOGU), Eskisehir, Türkiye | [2]Department of Chemistry, Eskisehir Osmangazi University (ESOGU), Eskisehir, Türkiye | [3]Department of Chemical Engineering, Istanbul Health and Technology University (ISTUN), Istanbul, Türkiye | [4]Advanced Materials Technologies Application and Research Center (IMATEK), Eskisehir Osmangazi University (ESOGU), Eskisehir, Türkiye | [5]Nanoscience and Nanotechnology, Graduate School of Natural and Applied Sciences, Eskisehir Osmangazi University (ESOGU), Eskisehir, Türkiye

Correspondence: Gulsah Yaman Uzunoglu (gulsah.uzunoglu@istun.edu.tr) | Recep Yuksel (recep.yuksel@ogu.edu.tr)

Received: 11 March 2026 | **Revised:** 1 May 2026 | **Accepted:** 14 May 2026

Keywords: chia seeds | dendrite suppression | hydrogel electrolyte | natural solvent | Zn-ion batteries

ABSTRACT

Natural solvent-based electrolytes are increasingly sought for zinc-ion batteries (ZIBs) as they provide a sustainable and cost-effective means to regulate water activity and electrode–electrolyte interfacial chemistry while retaining the intrinsic safety of aqueous systems. Herein, a sustainable electrolyte formulation utilizing a chia seed (CS)-based hydrogel is reported as an effective approach to improve the electrochemical stability of ZIBs. Owing to its high content of hydroxyl-rich polysaccharides and phenolic compounds, the chia seed-derived gel electrolyte (CSGE) tailors the Zn^{2+} solvation environment, decreases free-water activity, and restrains parasitic hydrogen evolution as well as dendritic zinc growth. Benefiting from this regulated solvation environment, the CSGE achieved a remarkably high Zn^{2+} transference number of 0.84. Consequently, Zn//Zn symmetric cells demonstrated outstanding electrochemical stability exceeding 4000 h at 1.0 mA cm^{-2} and 1.0 mAh cm^{-2}. Moreover, Zn//V_2O_5 cells achieved a high discharge capacity of 337.8 mAh g^{-1} at 0.1 A g^{-1} and maintained reliable rate performance between 0.2 and 10 A g^{-1}. In addition, ex situ SEM and XRD analyses revealed homogeneous deposition of Zn with a preferred (002) orientation. These findings demonstrate that electrolytes derived from renewable resources provide a cost-effective route for stable and sustainable ZIBs.

1 | Introduction

The rapid exhaustion of fossil fuels and growing environmental concerns have intensified international efforts toward renewable energy technologies. However, the intermittent nature of renewable energy sources such as solar and wind power necessitates the development of efficient, safe, and economically feasible energy storage systems [1, 2]. Although lithium-ion batteries (LIBs) currently dominate the energy storage market due to their high energy density and established manufacturing processes, challenges associated with lithium scarcity, high costs, safety risks, and environmental impacts drive the exploration of alternative battery chemistries, particularly for large-scale and stationary applications [3, 4].

Rechargeable aqueous zinc-ion batteries (ZIBs) have emerged as promising candidates for next-generation energy storage systems due to the natural abundance of zinc (Zn), its low redox potential (−0.76 V vs. SHE), high theoretical capacity, intrinsic safety, and environmental benignity [5, 6]. These merits make ZIBs particularly appealing for large-scale and stationary applications. However, despite these inherent advantages, the practical implementation of ZIBs is severely hindered by the poor reversibility and instability of the Zn metal anode in aqueous

environments. During repeated cycling, uneven Zn^{2+} ion flux and non-uniform electric-field distribution lead to localized Zn deposition, resulting in dendrite growth and premature cell failure. Simultaneously, the high chemical reactivity of Zn in aqueous electrolytes leads to parasitic side reactions, most notably the hydrogen evolution reaction (HER) and Zn corrosion, which significantly decrease Coulombic efficiency, interfacial stability, and long-term cycling performance [7, 8].

These challenges are fundamentally linked to the solvation chemistry of Zn^{2+} ions in aqueous electrolytes. It is widely recognized that the electrolyte's solvation structure has a pronounced effect on electrochemical interactions at the electrode–electrolyte interface [9, 10]. In conventional water-based electrolytes, Zn^{2+} ions are predominantly coordinated by water molecules, forming the hexacoordinated Zn^{2+}-aqua complex, while non-coordinated water molecules and anions remain outside the inner coordination sphere. The formation of this hydrated Zn^{2+} species imposes a substantial energetic barrier to Zn^{2+} desolvation, thereby promoting water-related parasitic side reactions. On the cathode side, unbound water molecules can penetrate and chemically attack both the host material and its discharge products, leading to material dissolution. On the anode side, HER activity is intrinsically unavoidable during Zn deposition, as water is thermodynamically unstable at the Zn plating potential. The generation of H_2 locally modifies the pH and triggers the buildup of insulating by-products, including zinc hydroxyl sulfates (ZHS), which impede ion and electron transport, decrease Zn and electrolyte concentrations, and accelerate Zn dendrite growth [9, 10]. Consequently, regulating the activity of water molecules is essential for controlling Zn^{2+} solvation-desolvation dynamics, thereby directly influencing the plating/stripping reversibility and electrochemical stability of the Zn anode [11]. Suppressing water-induced side reactions in aqueous electrolytes is therefore a critical prerequisite for achieving stable, reversible Zn plating/stripping at the Zn anode [12, 13].

In particular, compounds rich in hydroxyl (—OH) and carboxylic acid (—COOH) groups can disrupt the $[Zn(H_2O)_6]^{2+}$ solvation configuration through competitive hydrogen bonding, partially penetrating the inner coordination sphere and replacing coordinated H_2O molecules [14, 15]. Biomass-derived materials are inherently enriched with polar and hydrophilic functional groups, namely hydroxyl, amine, carboxylic acid, amide, and ether moieties, which can strongly interact with metal ions and dipolar molecules. The rich distribution of functional groups in biomass-based electrolyte systems enables regulation of Zn^{2+} solvation chemistry, reorganization of the interfacial double layer, and modulation of hydrogen-bond network dynamics, thereby suppressing the detrimental effects of non-coordinated water and aggressive anions. Furthermore, these functional moieties provide active sites that reconfigure and densify the hydrogen-bond network, promoting the formation of flexible hydrogel frameworks from biomass materials and imparting favorable mechanical compliance and interfacial adaptability for electrochemical energy storage applications [16–18]. Recent studies have demonstrated that green electrolyte additives, such as phytic acid [19], α-cyclodextrin [20], histidine [21], xylitol [22], and β-glycerophosphate disodium salt [22], can effectively regulate Zn^{2+} solvation, suppress parasitic reactions, and improve Zn deposition behavior in aqueous ZIBs. Beyond additive engineering, hydrogel electrolytes (HEs) provide an alternative strategy by restructuring the electrolyte environment through quasi-solid polymer networks, enabling regulated Zn^{2+} transport, reduced free-water activity, and improved interfacial stability. Biomass-derived hydrogels based on natural hydrogel species such as xanthan gum [22], gum arabic [23], cellulose [24], and gelatin have been widely explored as sustainable electrolyte matrices [25]. Nevertheless, most biomass-derived strategies rely on the isolation, purification, or incorporation of individual natural molecules as electrolyte additives, increasing processing complexity and limiting scalability. Consequently, the use of biomass as the primary electrolyte framework remains comparatively underexplored, despite its advantages of being non-toxic, biodegradable, and widely available, aligning with the growing demand for safe-by-design ZIBs. [16, 17, 26] Notably, in our previous work, Yuksel et al. demonstrated that an aloe vera-derived electrolyte containing 2.0 M $ZnSO_4$ can significantly extend the lifespan of Zn symmetric cells to 4600 h at a current density of 1.0 mA cm^{-2} by regulating Zn deposition and suppressing hydrogen evolution [27]. In a subsequent work, a flaxseed-derived electrolyte enabled long-term highly reversible Zn deposition and dissolution exceeding 3000 h at 1.0 mA cm^{-2}, while exhibiting substantially high Zn^{2+} transference number ($t_{Zn}{}^{2+}$) and rate capability [28]. From this perspective, replacing DI water in the electrolyte with sustainable, natural, and environmentally benign biomass extracts represents a more fundamental and promising strategy to mitigate water-induced side reactions while preserving ionic conductivity and electrochemical reversibility. Such a solvent-formulating approach offers a viable pathway toward greener, scalable, and intrinsically stable ZIB systems.

Building on this concept, herein we explore chia seeds (*Salvia hispanica L.*) as another sustainable biomass resource that can serve as a biomass-derived natural solvent for hydrogel electrolyte formulations. Chia seeds are widely used in the food and animal feed industries as a nutrient-rich resource, and their global production has increased owing to their recognized health benefits and growing popularity. They contain significant amounts of unsaturated fatty acids (e.g., linolenic acid), dietary fiber, proteins, and natural antioxidants such as phenolic glycosides Q and K, chlorogenic acid, caffeic acid, quercetin, and kaempferol [29]. Chia seed–derived hydrogel (mucilage) has received increasing attention due to its abundant organic constituents and amphipathic characteristics [29]. When chia seeds are soaked in water at room temperature, a hydrogel is formed with a diverse range of organic constituents, including phenolic compounds bearing carboxylic acid functionalities along with quercetin, phenolic glycosides, and various monosaccharides, including glucose, galactose, arabinose, and xylose [30, 31]. The phenolic acids and carbohydrate derivatives embedded within the chia seed mucilage matrix are enriched with hydroxyl, ether, and carboxylate functional groups. These functionalities are essential for coordinating Zn^{2+} ions, suppressing hydrogen evolution, and mitigating dendritic Zn deposition [32]. Accordingly, incorporating chia seed hydrogel into electrolyte systems offers a promising strategy to modulate the Zn^{2+} coordination environment, suppress parasitic reactions, and stabilize the electrode–electrolyte interface. To date, chia seed-derived mucilage has been reported only as a gel electrolyte for flexible supercapacitors, where it exhibited favorable rheological properties, electrochemical stability, and long cycling life. However, its application has been restricted to electrostatic

charge storage and low-voltage operation, without involvement in metal-ion redox chemistry [33]. Accordingly, the potential of chia seed hydrogel to regulate Zn^{2+} solvation and stabilize Zn metal anodes in ZIBs has yet to be elucidated.

In this work, a chia seed–derived gel electrolyte (CSGE) was formulated by directly dissolving $ZnSO_4$ into a chia seed hydrogel, yielding a 2.0 M electrolyte while retaining high ionic conductivity. Unlike conventional additive-based strategies, this approach leverages the inherent molecular complexity of the biomass-derived hydrogel as a multifunctional electrolyte matrix, eliminating the need for synthetic or isolated additives. Obtaining natural electrolytes in gel form is very important because biomass-derived hydrogel electrolytes can form mechanically robust ion-conduction pathways, leading to improved interfacial stability and enhanced electrochemical performance while offering intrinsic sustainability advantages [34]. Notably, the CSGE exhibits a substantially high t_{Zn}^{2+} of 0.84 and enables electrochemically stable Zn plating/stripping behavior exceeding 4000 h in Zn//Zn symmetric cells. Moreover, Zn//V_2O_5 cells employing CSGE deliver a high specific discharge capacity of 337.8 mAh g^{-1} at 0.1 A g^{-1}, together with stable rate performance and long-term cycling stability. Structural and morphological analyses confirm a dense, well-distributed Zn metal buildup, with a preferential Zn(002) crystal plane and suppressed dendritic growth. Overall, this work establishes biomass-derived hydrogels as scalable and sustainable electrolyte platforms for stabilizing Zn interfaces in advanced aqueous battery systems.

2 | Results and Discussion

Figure 1a illustrates the process of fabricating the chia seed-based gel electrolyte (CSGE) for ZIBs. For CS hydrogel preparation, 1.0, 5.0, and 10.0 g of commercial chia seeds were immersed in 100 mL of DI water at ambient temperature, yielding viscous, transparent hydrogels with varying extract concentrations, labeled CSG-1, CSG-5, and CSG-10, respectively. The resulting hydrogels were directly employed for the preparation of gel electrolytes for ZIBs without further purification.

FTIR spectroscopy was conducted on the freeze-dried CS aerogel (Figure S1) to probe the functional groups governing coordination interactions and hydrogen-bond formation within the CS hydrogel matrix. The resulting spectrum exhibits vibrational signatures consistent with phenolic acid moieties and carbohydrate-derived structures, closely matching the spectral profile previously reported for the flaxseed aerogel in our earlier study (Figure 1b) [35]. Taken together, these observations indicate that the CS hydrogel framework contains phenolic and carbohydrate-derived molecules bearing hydroxyl and carbonyl functionalities, which cooperatively establish an extensive hydrogen-bonding network [36]. To gain deeper insights into the regulation of Zn^{2+} solvation and water activity, Raman and FTIR analyses were performed (Figures S3–S5). In the Raman spectrum of the 2.0 M $ZnSO_4$ aqueous electrolyte (AE), an intense peak corresponding to SO_4^{2-} is observed at 980 cm^{-1}, alongside characteristic O—H stretching modes, which are a symmetric mode at 3280 cm^{-1} and an asymmetric mode at 3410 cm^{-1} [37, 38]. In contrast, for the CS-based gel electrolyte (CSGE), while the sulfate peak remains, the intensities of the O—H stretching modes in the 3000–3700 cm^{-1} region are significantly suppressed. The obtained Raman results show that CSGE inhibits free-water molecules and enhances the stability of ZIB devices. The characteristic O—H vibration bands of water molecules show a clear redistribution of intensities among the different hydrogen-bonded species. Specifically, the decrease in the intensity of the band associated with water indicates that the CSGE matrix disrupts the hydrogen-bonding structure of water, integrating water molecules into the hydrogel framework. This is further supported by FTIR analysis, where shifts in the O—H stretching band of CSGE indicate intermolecular interactions between the water molecules and the functional groups of the chia seed mucilage. This molecular-level regulation is consistent with the enhanced electrochemical stability and suppressed hydrogen evolution observed in CSGE-based cells.

Enhanced wettability of the metal anode by the electrolyte plays a pivotal role in metal-based batteries, as it reduces the nucleation overpotential, increases the density of nucleation sites, and promotes a more homogeneous distribution of cations at the anode surface. This improved interfacial contact supports the formation of thin and robust solid–electrolyte interphase (SEI) layers, effectively suppressing dendritic growth and thereby enhancing cycle stability and operational safety [39, 40]. In this regard, the extent of wettability offers valuable information regarding the interaction between the electrolyte and the electrode, which significantly affects the nucleation of Zn and its corrosion characteristics [41, 42]. In order to assess the wettability of the Zn anode, contact angles of both aqueous electrolyte (AE) and CSGE were measured as provided in Figure 1c. The measured contact angle for AE was 99.94°, whereas CSGE exhibited a lower value of 90.29°, indicating stronger interfacial interaction with the Zn surface. This improved wettability is likely associated with the adsorption of hydrophilic hydroxyl moieties and zincophilic functionalities in the CSGE electrolyte matrix onto the Zn anode surface. Such interfacial interactions contribute to a more uniform electric-field distribution and facilitate the formation of a dynamic protective interphase [43].

To elucidate the influence of CS content and $ZnSO_4$ concentration on the electrolyte properties, the pH and ionic conductivity of neat CS hydrogels prepared with different seed loadings were systematically compared with those of CS-based gel electrolytes containing three different $ZnSO_4$ concentrations. CSG-5 exhibited a pH value of 5.75, while the pH value decreased to 4.48 upon incorporation of 2 M $ZnSO_4$. This pH reduction is attributed to the $ZnSO_4$ salt rather than the CS hydrogel matrix, as the aqueous 2 M $ZnSO_4$ electrolyte exhibited a comparable pH value of 4.42. At nearly all $ZnSO_4$ concentrations, the CS-based gel electrolytes exhibited a slight increase in pH. This behavior is associated with the chelation of Zn^{2+} ions by phenolic acids within the CS hydrogel, resulting in the formation of carboxylate and phenoxide coordination complexes accompanied by proton release into the electrolyte (Figure S2) [44].

Ionic conductivity measurements of the pristine CS-hydrogels were performed by means of an ionic conductivity probe. As shown in Figure 1d, CSG-1, CSG-5, and CSG-10 exhibited ionic conductivities of 0.116, 0.361, and 0.625 mS cm^{-1}, respectively. This evident enhancement in ionic conductivity with increasing chia seed content can be explained by the greater number of polar functional groups, including carboxylic acid, carbonyl, hydroxyl,

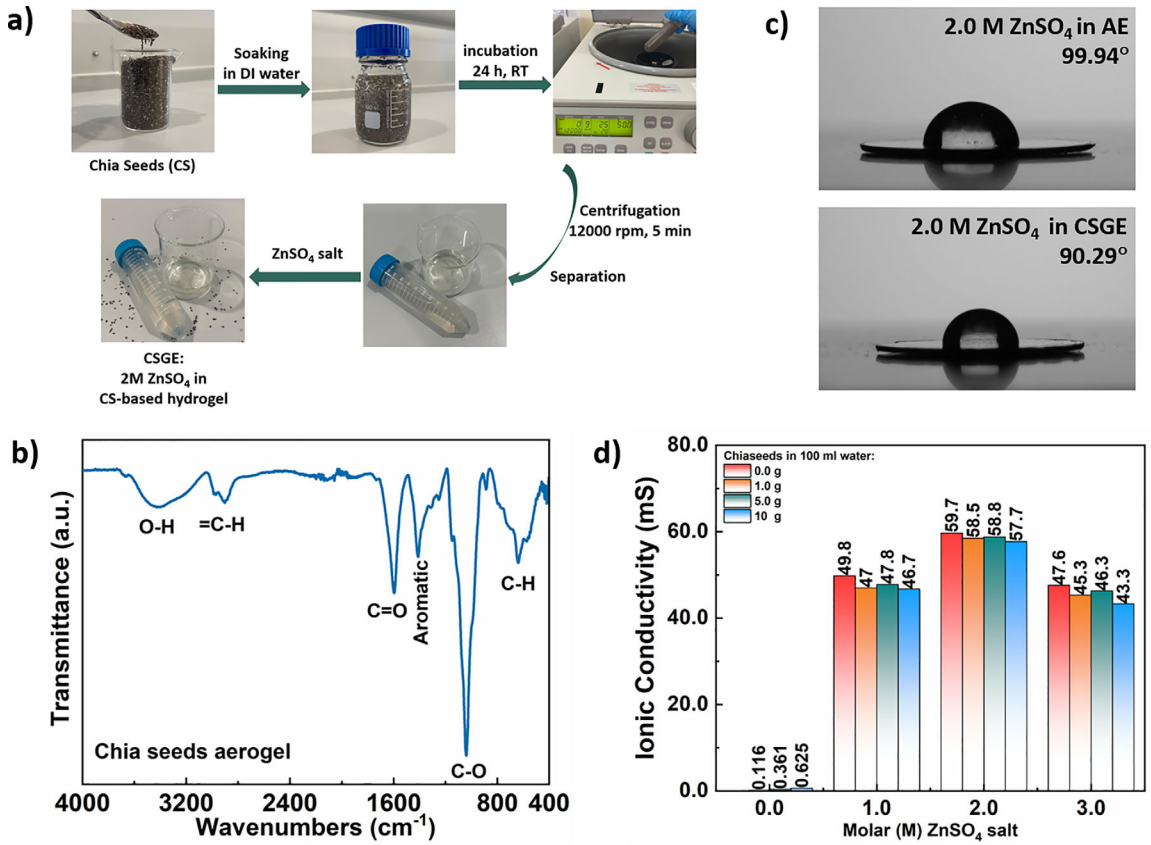

FIGURE 1 | Preparation of CS-based gel electrolyte (CSGE). (a) Schematic illustration of CSGE electrolyte formulation. (b) FTIR spectrum of the aerogel derived from CS. (c) Results of the contact angle measurements. (d) Ionic conductivities at various concentrations.

and ether moieties, which dissolve into the aqueous phase and thus facilitate ion transport throughout the hydrogel matrix. It is important to note that, even without the addition of $ZnSO_4$, the CS-hydrogel exhibits sufficient intrinsic ionic conductivity to function as an electrolyte medium. Nevertheless, introducing $ZnSO_4$ strengthens ionic transport properties and enables stable and reversible Zn deposition/dissolution processes, which are critical for the long-term performance of the rechargeable battery systems [45]. Following the incorporation of Zn salt, the CS-hydrogel retained its viscous gel-like structure across the entire salt concentration range from 1 to 3 M, suggesting that the intrinsic hydrogen-bonded network of the CS-hydrogel matrix remained intact. The resulting CS-based electrolytes exhibited high compositional uniformity and robustness, suggesting effective dissolution and uniform distribution of Zn^{2+} ions throughout the hydrogel. Figure 1d illustrates the ionic conductivity of the CS-based gel electrolytes measured at ambient temperature, including the CSGE formulation, denoted as the CS electrolyte containing 2 M $ZnSO_4$. The measured ionic conductivities of the CS-based gel electrolytes ranged from 43.7 to 58.8 mS cm^{-1}. Notably, raising the concentration of $ZnSO_4$ from 1 to 2 M yielded an approximately 25% enhancement in ionic conductivity. In contrast, a reduction in ionic conductivity was observed when the $ZnSO_4$ concentration was further increased to 3 M for all investigated CS contents. This behavior indicates a trade-off between the higher concentration of charge carriers and diminished ionic mobility arising from intensified interionic electrostatic interactions and partial complexation of Zn^{2+} ions with polar, hydrophilic organic constituents of the CSGE matrix. This behavior is consistent with reports on concentrated aqueous electrolytes, where ionic conductivity diminishes at elevated salt concentrations because of stronger interionic interactions and ion-pair/aggregate formation that impede ion transport [46, 47]. Based on these observations, CSGE containing 2 M $ZnSO_4$ was identified as the optimal formulation and was employed for all subsequent electrochemical evaluations in this study.

To investigate the compatibility of the CSGE formulation and its stabilizing effect on the electrochemical behavior of the Zn anode, electrochemical stability tests were performed. Additionally, Zn interfacial stability and suppression of parasitic side reactions were evaluated through various stability measurements in aqueous electrolyte (Figure 2). When operated at 1.0 mA cm^{-2} (1.0 mAh cm^{-2}), the CSGE-based cell achieved stable cycling for over 4000 h (Figure 2a). The initial overpotential of CSGE is around 56 mV, then increases to ~100 mV and stabilizes at ~50 mV around 2700 h. Remarkably, while the cell with AE exhibited an abrupt voltage drop after ~400 h, indicating a dendrite-induced short circuit, the CSGE-based cell maintained reversible Zn plating and stripping efficiency. To assess the robustness of CSGE under more demanding cycling conditions, additional electrochemical tests were conducted under intensified cycling. Figure 2b compares the cycling behavior of symmetric Zn//Zn cells using AE and CSGE under a current density of 2.0 mA cm^{-2} with an areal capacity of 2.0 mAh cm^{-2}. The cell employing AE rapidly encountered a short circuit and cell failure after 139 cycles (278 h), indicating severe instability at the Zn metal anode interface. Nevertheless, the CSGE-based cell displayed superior

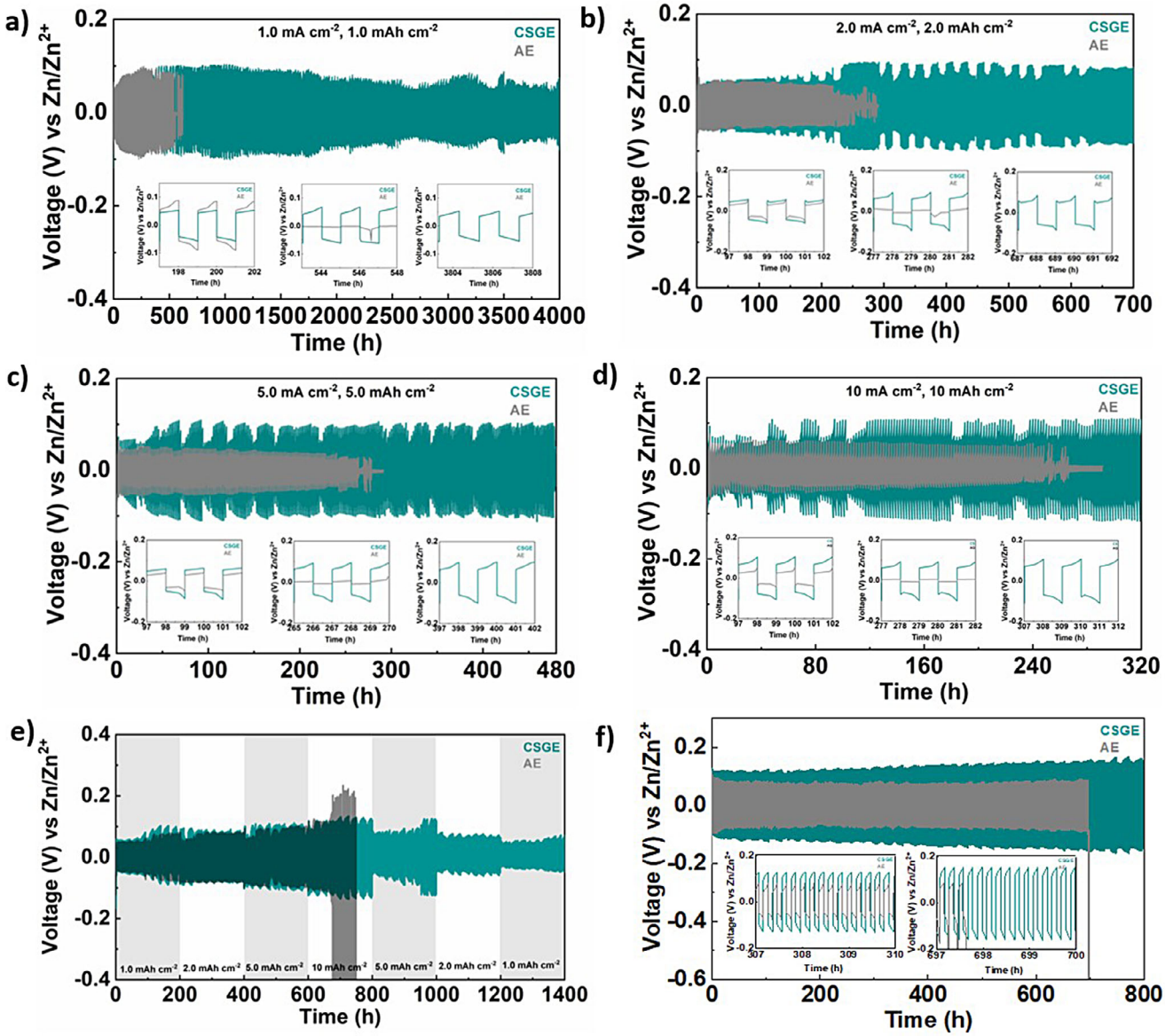

FIGURE 2 | Plating/stripping performance of Zn//Zn symmetric cells with AE and CSGE under progressively increasing current densities and areal capacities: (a) 1.0 mA cm^{-2} (1.0 mAh cm^{-2}), (b) 2.0 mA cm^{-2} (2.0 mAh cm^{-2}), (c) 5.0 mA cm^{-2} (5.0 mAh cm^{-2}), and (d) 10 mA cm^{-2} (10 mAh cm^{-2}). (e) Rate capability across current densities between 1.0 and 10 mA cm^{-2} (1.0–10 mAh cm^{-2}). (f) GCD curves at 10 mA cm^{-2} with an areal capacity of 1.0 mAh cm^{-2}.

long-term cycling durability, operating stably for more than 700 h. Within the first 132 h, the CSGE cell exhibited a relatively modest overpotential of approximately 50 mV, comparable to that of the AE cell. With continued cycling, the overpotential gradually increased to around 90 mV and subsequently stabilized, fluctuating between ~60 and ~90 mV during prolonged operation. The sustained stability over 700 h confirms that the CSGE effectively mitigates parasitic reactions while enabling remarkably reversible Zn plating and stripping.

Further evaluation at 5.0 mA cm^{-2} (5.0 mAh cm^{-2}) confirmed the superior electrochemical performance of CSGE (Figure 2c). Although the AE-based cell initially showed a slightly reduced overpotential of about 40 mV, it failed after 133 cycles (265 h). By comparison, the CSGE-based cell maintained stable operation for up to 480 h, with the overpotential varying between ~65 and 100 mV, demonstrating enhanced electrochemical durability under more demanding cycling conditions.

To evaluate performance under extreme operating conditions relevant to high-power systems, electrochemical stability tests were performed at elevated current densities. Under a current density of 10.0 mA cm^{-2} (10.0 mAh cm^{-2}), the Zn//Zn cell using AE experienced short-circuiting after 267 h. (Figure 3d). Conversely, the Zn//Zn cell utilizing CSGE sustained stable operation for over 320 h, indicating excellent reversibility and stability of the Zn plating/stripping process. Notably, the relatively small increase in overpotential observed for CSGE at higher current densities can be attributed to the formation of a dense, homogeneous Zn layer, which enhances charge transfer and alleviates polarization at the Zn anode interface [48]. As shown in Figure 2e, the symmetric cells were evaluated under stepwise current densities.

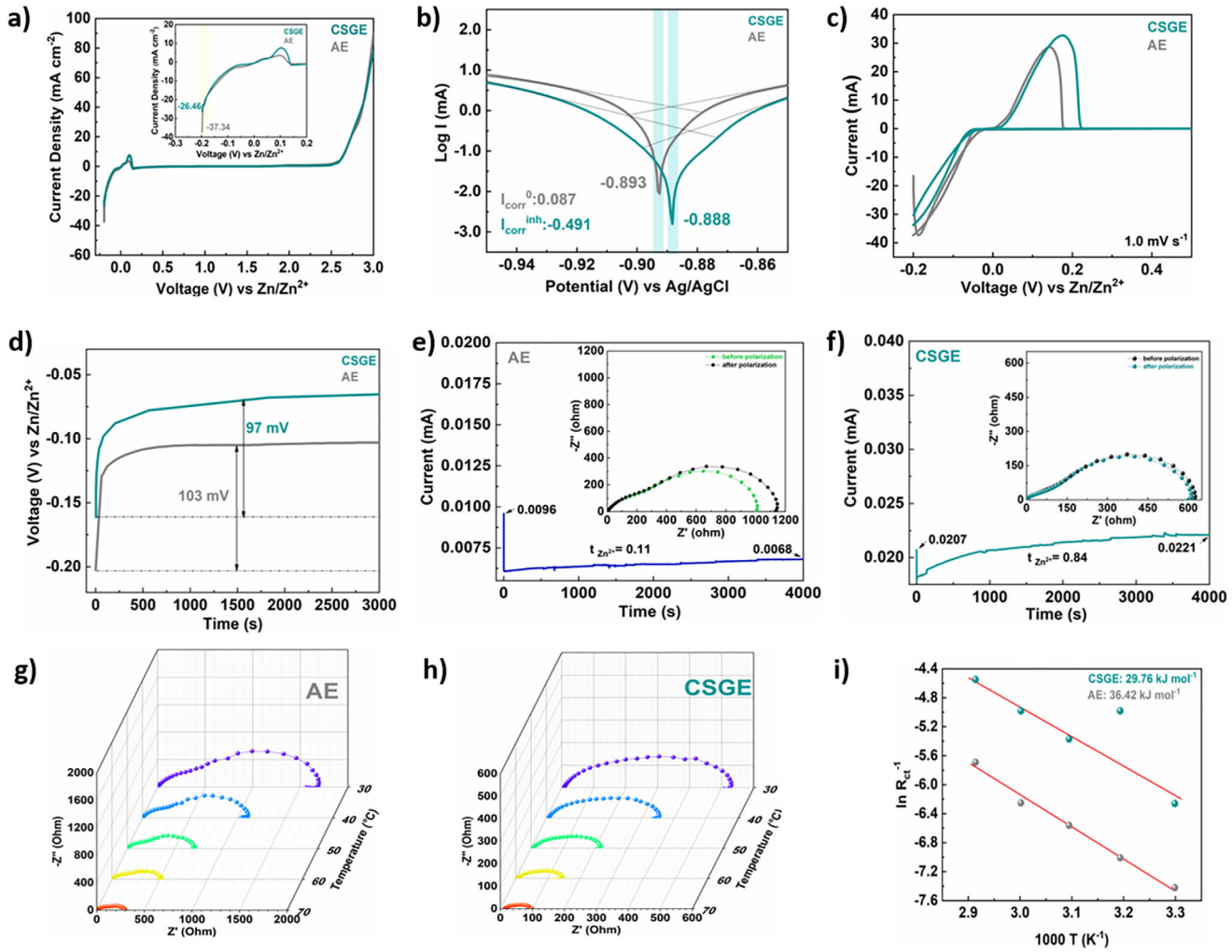

FIGURE 3 | Electrochemical characterizations. (a) Linear sweep voltammetry (LSV) curves and (b) corresponding Tafel plots of AE and CSGE recorded at a scan rate of 1.0 mV s^{-1}. (c) Cyclic voltammetry (CV) profiles of AE and CSGE electrolytes in Zn//Cu cells measured at 1.0 mV s^{-1}. (d) Zn nucleation overpotential profiles. Chronoamperometry responses and EIS spectra collected before and after DC polarization for (g) AE and (h) CSGE. (i) Activation energy (E_a) plots.

The current density was progressively raised from 1 to 10 mA cm^{-2} (1-10 mAh cm^{-2}) every 200 h, followed by a reverse sequence. In this test, the AE-based cell failed after 666 h due to severe dendrite growth, whereas the CSGE-based cell maintained stable cycling with a nearly constant overpotential for over 1400 h. The advantage of using CS hydrogel as a natural solvent is especially apparent under demanding conditions, where dendrite suppression and interfacial stability are critical [49, 50]. Figure 2f shows that the CSGE-based cell sustained reversible cycling for more than 800 h at 10 mA cm^{-2} with an areal capacity of 1.0 mAh cm^{-2}, demonstrating its good ability to maintain interfacial integrity and suppress uncontrolled Zn growth under aggressive plating/stripping conditions [51]. Conversely, the symmetric cell with the aqueous electrolyte showed inferior cycling durability and underwent a dendrite-induced short circuit after 697 h. Table S1 compares the electrochemical stability of the CSGE reported here with representative aqueous ZIB electrolytes incorporating bio-derived solvents or additives. The superior cycling durability achieved with the CSGE highlights its substantial potential as an economically viable, environmentally benign, and sustainable electrolyte system for advanced Zn-based battery technologies.

To probe CSGE's ability to suppress HER and enhance the interfacial stability of the Zn anode, a series of electrochemical tests was performed. The electrochemical stability window (ESW) and hydrogen evolution behavior of CGSE were investigated using linear sweep voltammetry (LSV). As presented in Figure 3a, at a potential of −0.197 V, the aqueous electrolyte exhibits a higher cathodic current density (−37.34 mA cm^{-2}) than CSGE (−26.46 mA cm^{-2}). The suppressed current response observed in the CSGE system indicates effective HER suppression. Potentiodynamic polarization measurements further elucidate the corrosion behavior of Zn anodes, and the corrosion current values of both electrolytes were calculated from the Tafel plots (Figure 3b). The Zn anode in the CSGE system displays a slightly more positive corrosion potential (E_{corr} = −0.888 V vs. Ag/AgCl) than that measured in AE (−0.893 V vs. Ag/AgCl). Moreover, the corrosion current density of the 2.0 M $ZnSO_4$ aqueous electrolyte reaches 0.174 mA cm^{-2}, whereas a lower value of

−0.982 mA cm^{-2} is observed for the CSGE. The simultaneous positive shift in E_{corr} and pronounced decrease in I_{corr} indicate substantially suppressed anode corrosion, which is attributed to the formation of a stabilized interfacial layer induced by the CS-hydrogel-containing electrolyte [52, 53].

Cyclic voltammetry (CV) experiments were conducted at 1.0 mV s^{-1} utilizing asymmetric Zn//Cu cells to examine the nucleation overpotential of Zn^{2+} on the Zn anode. Cu foil was used as the working electrode, while Zn foil served as the counter and reference electrodes. As illustrated in Figure 3c, both AE and CSGE display unique and reversible redox peaks that are associated with the Zn plating and stripping processes. This observation confirms their electrochemical reversibility and suggests that the organic moieties within the CS-hydrogel do not undergo redox reactions during Zn plating and stripping. The CSGE electrolyte delivers a higher cathodic current density, indicating accelerated Zn^{2+} transport kinetics compared with AE [19, 54, 55]. Coulombic efficiency measurement results of the asymmetrical cells using formulated electrolytes were provided in Figures S6 and S7. Furthermore, the nucleation overpotential was assessed in Zn//Cu cells with an applied current density of 1.0 mA cm^{-2}. As illustrated in Figure 3d, the nucleation overpotential (NOP) was reduced from 103 mV for AE to 97 mV for CSGE, demonstrating rapid Zn^{2+} transport at the Zn/electrolyte interface. This reduced overpotential arises from the weakened hydration environment in the CSGE electrolyte, which lowers the desolvation energy barrier for Zn^{2+} and facilitates homogeneous Zn nucleation. The zincophilic species introduced by the CSGE system regulate the Zn^{2+} solvation structure, thereby promoting uniform nucleation behavior [56, 57].

The Zn^{2+} transference number ($t_{Zn}{}^{2+}$) is a critical indicator of ion transport behavior at the anode/electrolyte interface. Symmetric Zn//Zn cells were employed to determine $t_{Zn}{}^{2+}$ values for both electrolytes, with chronoamperometry profiles and electrochemical impedance spectroscopy (EIS) spectra collected before and after dc polarization. As shown in Figure 3e,f, the $t_{Zn}{}^{2+}$ value calculated from these measurements is 0.84 for the CSGE electrolyte, significantly higher than 0.11 for AE. This substantial increase in $t_{Zn}{}^{2+}$ with CSGE reflects more efficient Zn^{2+} transport and reduced anion mobility, consistent with the presence of hydrogen-bonding networks and zincophilic functional groups that tailor the solvation structure and minimize parasitic reactions at the anode (Table S2) [48, 54, 58]. To further elucidate the desolvation process of Zn^{2+}, the activation energy (E_a) was also studied, which is linked to the mass transfer kinetics of Zn^{2+} at the anode/electrolyte interface, thus affecting the deposition behavior of Zn^{2+}. The Arrhenius equation was used to determine the activation energy: E_a: $\frac{1}{R_{ct}} = Aexp(\frac{E_a}{RT})$, where R_{ct} indicates the charge-transfer resistance and R represents the ideal gas constant. Accordingly, temperature-dependent EIS measurements were performed on Zn//Zn symmetric cells containing AE and CSGE electrolytes. As shown in Figure 3g (AE) and h (CSGE), the semicircle diameter in the Nyquist plots consistently decreases with increasing temperature, reflecting a decrease in R_{ct}. According to the fitting results based on the Arrhenius formula (Figure 3i), the calculated activation energies were 36.42 kJ mol^{-1} for AE and 29.72 kJ mol^{-1} for CSGE. The lower activation energy in CSGE confirms more favorable Zn^{2+} transport and accelerated Zn deposition kinetics [56, 59].

To elucidate Zn deposition behavior in CSGE, the morphology of cycled Zn anodes was examined by ex situ SEM. As shown in Figure 4a, the Zn anode cycled in AE exhibits pronounced multidirectional dendrites and flake-like deposits with hexagonal morphology, indicating unstable interfacial behavior accompanied by uneven Zn nucleation throughout repeated cycling. In contrast, the Zn anode after cycling in CSGE exhibits a smooth, compact surface morphology, suggesting uniform Zn deposition and stable Zn plating/stripping behavior (Figure 4b). In addition, ex situ energy dispersive spectroscopy (EDS) analysis of the Zn anode retrieved from the Zn//Zn cell after cycling with CSGE further revealed a uniform distribution of C, S, and O elements on the anode surface (Figures S8 and S9). This observation suggests the formation of an in situ–generated SEI layer during cycling. This interfacial layer may originate from the adsorption and coordination of dipolar organic molecules within CSGE onto the Zn anode surface. Ex situ XRD analysis of cycled Zn anodes further corroborates the morphological differences and reveals electrolyte–Zn crystal-plane interactions at the interface. As shown in Figure 4c, both CSGE and AE display characteristic Zn diffraction peaks. The (002)/(100) peak intensity ratio ($I_{(002)}/I_{(100)}$) offers valuable information regarding the preferential deposition of Zn [60, 61]. An increase in the $I_{(002)}/I_{(100)}$ ratio from 0.660 for AE to 1.157 for CSGE, indicating a preferential Zn deposition along the (002) crystallographic plane. Preferential (002) growth is widely associated with dense, planar Zn deposition and suppressed dendrite growth [15, 62]. These findings confirm that CSGE induces (002)-oriented Zn growth and controlled Zn^{2+} ion transport, leading to dendrite-free deposition, improved interfacial stability, and remarkably enhanced cycling durability of Zn anodes.

In-operando optical microscopy was used to observe Zn deposition and concurrent HER activity by tracking the morphological evolution during plating [63]. The Zn deposition was conducted at 5.0 mA cm^{-2} for 60 min. Figure 4d shows that the Zn anode after cycling in CSGE maintained a dense, smooth surface throughout the plating process, exhibiting no discernible dendritic features. In contrast, AE showed dendrite nucleation within 20 min, evolving into large, irregular dendrites at the end of 60 min.

Figure 4e illustrates a schematic comparison of Zn deposition in AE and CSGE, which correlates well with the ex situ SEM and XRD findings. In AE, Zn deposition is highly uneven, leading to non-uniform crystal orientations and pronounced dendritic growth along the Zn(100) plane, consistent with ex situ characterization. Conversely, CSGE induces a compact, homogeneous Zn deposition with a dominant Zn(002) texture, in agreement with the dendrite-free surface morphology revealed by SEM and XRD. Collectively, these results indicate that incorporating the CS-hydrogel as a natural solvent promotes the synergistic formation of an in situ SEI layer and regulates the Zn^{2+} coordination environment at the Zn/electrolyte interface. This interfacial regulation moderates local electric-field distribution and Zn^{2+} flux, thereby facilitating more uniform Zn nucleation and growth [19, 64].

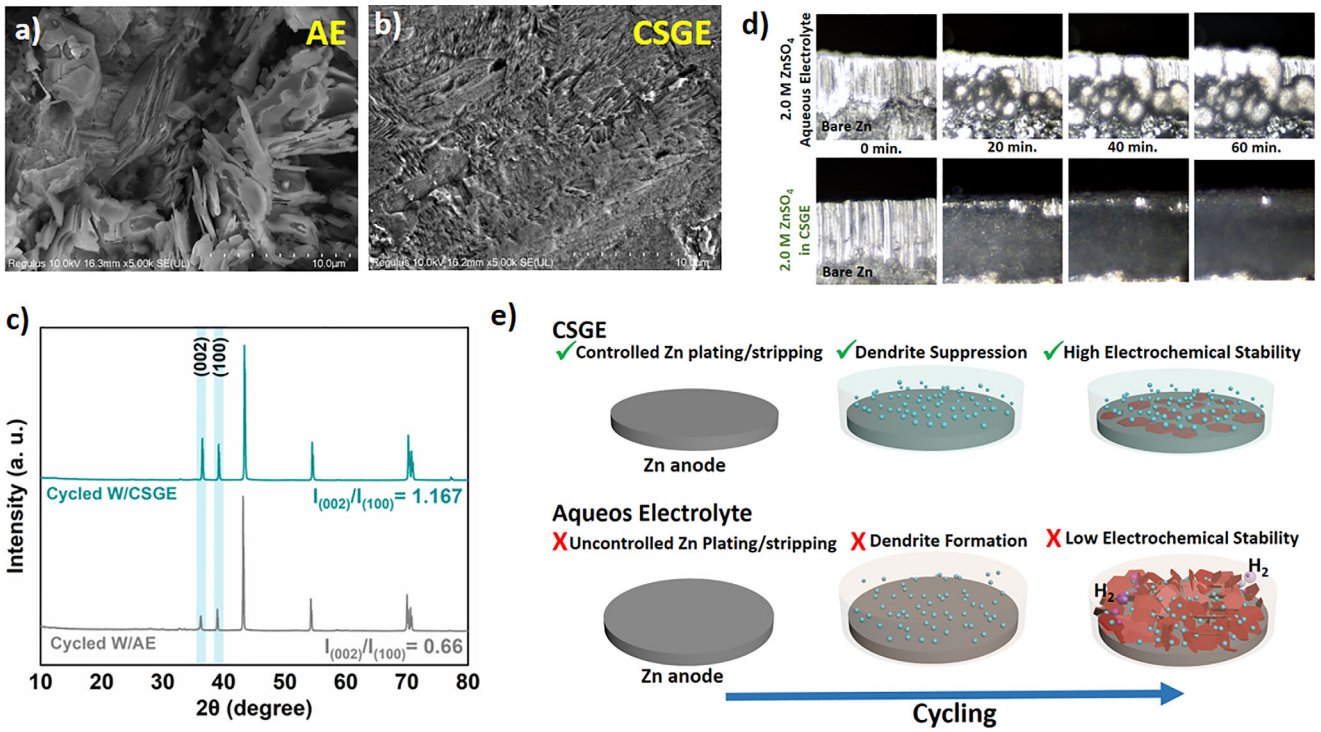

FIGURE 4 | Morphology of Zn anodes after cycling in (a) AE and (b) CSGE, revealed by ex situ SEM. (c) XRD patterns of the corresponding cycled Zn electrodes. (d) In-operando optical microscopy snapshots of Zn plating in AE and CSGE. (e) Schematic illustration comparing Zn deposition mechanisms on Zn anodes in AE and CSGE.

The electrochemical behavior of the CSGE was further evaluated in a full ZIB configuration employing vanadium pentaoxide nanowires (V_2O_5 NWs) as the cathode. Structural and morphological details regarding the V_2O_5 NWs are provided in Figures S10–S13. The CV profiles of ZIBs assembled with the CSGE and AE were collected at 0.1 mV s^{-1} within 0.2–1.6 V (Figure 5a). In both systems, two well-defined pairs of anodic and cathodic peaks characteristic of the V_2O_5 cathode are observed, indicating that the use of CSGE does not alter the intrinsic redox chemistry. The oxidation peaks centered at 0.758 and 0.984 V correspond to the V^{4+}/V^{5+} and V^{3+}/V^{4+} redox transitions, respectively, while the reduction peaks at 0.845 and 0.593 V arise from the V^{5+}/V^{4+} and V^{4+}/V^{3+} processes, respectively. By comparison, AE exhibits redox couples at 0.751/0.596 and 0.982/0.841 V. Notably, the oxidation peak at 0.984 V in the CSGE-based cell shows a slight anodic shift (~2 mV) relative to AE. Moreover, CSGE-based displays a larger integrated CV area and enhanced redox peak intensity, suggesting improved Zn^{2+} storage capability of the V_2O_5 cathode without compromising redox reversibility [65].

To investigate the electrochemical kinetic response of both electrolytes, CV measurements were performed at potential sweep rates between 0.1 and 1.0 mV s^{-1} (Figure 5b for CSGE and Figure S14 for AE). Upon increasing the scan rate, the anodic peaks shifted to more positive potentials, whereas the cathodic peaks shifted to more negative potentials. At the same time, current densities of the redox peaks and the potential difference between oxidation and reduction peaks increased for both electrolytes. This behavior is associated with stronger charge polarization at the electrode interface during rapid potential sweeps. To further elucidate charge-storage mechanisms associated with the electrolyte systems, the fraction of surface-controlled capacitive processes was analyzed using CV profiles collected under varying scan rates (Figures S15 and S16). Moreover, b-values were determined to quantitatively distinguish the contributions of diffusion-controlled and surface-capacitive processes in the overall Zn^{2+} storage behavior of the fabricated ZIBs. Figure 5c shows the calculated b-values belonging to the peaks O1, O2, R1, and R2 in the CSGE-based cell, which are 0.671, 0.886, 0.818, and 0.652, respectively. The corresponding values for the AE-based cell are presented in Figure S17. The variation in b-values among different redox peaks indicates that a combination of bulk Zn^{2+} diffusion and surface-controlled capacitive kinetics governs the charge-storage process [28]. Notably, the relatively high b-values for peaks O2 and R1 suggest a dominant surface-capacitive contribution, reflecting accelerated interfacial charge-transfer kinetics and reduced Zn^{2+} desolvation barriers in the presence of the CSGE electrolyte. Such kinetic enhancement is consistent with the improved rate capability and reduced polarization observed for the CSGE-based full cells. To further elucidate the influence of CSGE on Zn^{2+} transport kinetics within the V_2O_5 NW cathode, galvanostatic intermittent titration technique (GITT) measurements were performed to evaluate the apparent Zn^{2+} diffusion behavior. CSGE exhibits a higher apparent Zn^{2+} diffusion coefficient ($D_{Zn^{2+}} = 2.80 \times 10^{-9} cm^2\ s^{-1}$) than AE ($D_{Zn^{2+}} = 2.36 \times 10^{-9} cm^2\ s^{-1}$), demonstrating that employing the CS-hydrogel as the solvent matrix enhances Zn^{2+} transport (Figure S18). This trend is likely associated with alterations in the Zn^{2+} solvation environment in CSGE, which may reduce anion mobility and facilitate cation migration, in line with observations reported for hydrogen-bond-regulated electrolyte systems [26, 66].

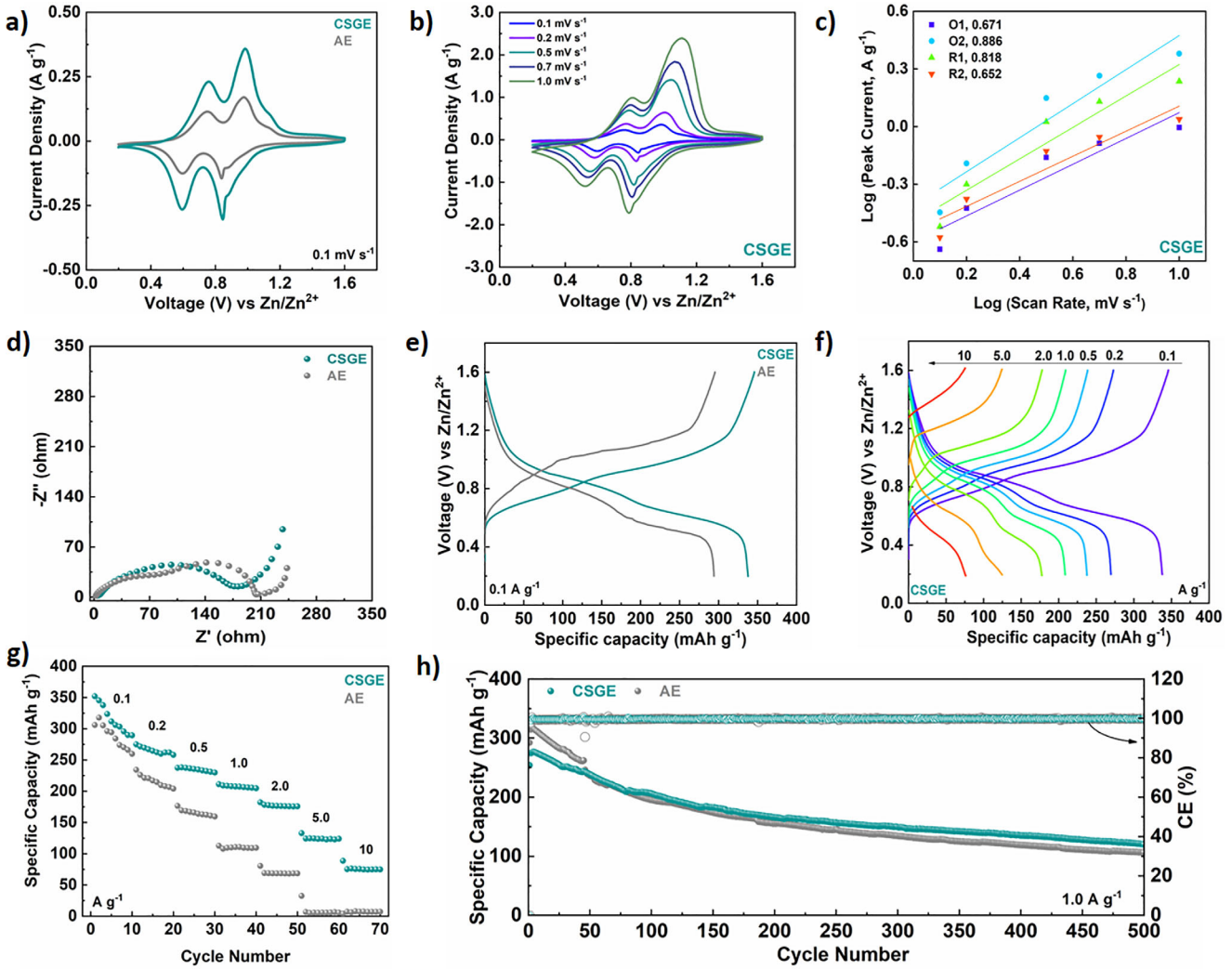

FIGURE 5 | Electrochemical behavior of ZIBs using V_2O_5 nanowire cathodes with AE and the biomass-derived CSGE system. (a) Comparison of cyclic voltammetry responses recorded at 0.1 mV s^{-1}. (b) CV profiles of the CSGE-based cell measured at different scan rates. (c) Linear fitting plots of log(i) vs. log(v) for anodic and cathodic peaks. (d) Electrochemical impedance spectra (Nyquist plots). (e) Galvanostatic charge–discharge profiles obtained at 0.1 A g^{-1}. (f) GCD profiles of the ZIB with CSGE under different current densities. (g) Rate capability of ZIBs employing the formulated electrolytes. (h) Cycling stability of cells using AE and CSGE at 1.0 A g^{-1}.

EIS was employed to investigate the impact of replacing DI water with CS-hydrogel on the electrochemical behavior of ZIBs, from which the charge-transfer resistance (R_{ct}) values of the V_2O_5//Zn cells were determined. The corresponding series resistance (R_s) values for the ZIB cells assembled with CSGE and the aqueous electrolyte were determined to be 1.95 and 1.88 Ω, respectively, indicating comparable bulk ionic transport in both systems. The R_{ct} value, extracted from the high-frequency semicircle of the Nyquist plot, was significantly lower for the CSGE-based cell (174.7 Ω) than for the AE cell (200.9 Ω), as shown in Figure 5d. The reduced R_{ct} associated with CSGE reflects improved interfacial charge-transfer kinetics, which can be attributed to the regulated Zn^{2+} solvation structure, reduced water activity, and stabilized electrode/electrolyte interface provided by the CS-hydrogel matrix. Conversely, AE facilitates parasitic reactions, including hydrogen evolution and corrosion, leading to an increase in R_{ct} due to the generation of insulating by-products. Preventing these parasitic reactions can significantly reduce surface passivation [67], thereby improving interfacial charge transfer, reflected by lower R_{ct} [48]. As a result, CSGE facilitates rapid interfacial charge transfer and improved Zn plating/stripping behavior.

Galvanostatic charge–discharge (GCD) measurements were carried out to evaluate the charge-storage performance and rate capability of ZIBs employing CSGE at current densities ranging 0.1 and 10 A g^{-1}. As illustrated in Figure 5e, the V_2O_5/Zn cell employing CSGE delivered a high specific discharge capacity of 337.8 mAh g^{-1} at 0.1 A g^{-1}, which is substantially higher than the 294.0 mAh g^{-1} achieved with AE. Across various current densities, the CSGE-based cell consistently exhibited higher specific capacities compared to its aqueous counterpart (Figure 5f and Figure S19). The corresponding GCD profiles (Figure 5g) reveal that the ZIB using CSGE maintains stable discharge capacities across the entire current range, preserving a relatively high capacity output. In contrast, the cell employing AE shows markedly lower capacities and fails to deliver measurable discharge capacity at high current densities of 5.0 and

10 A g^{-1}. Table S3 summarizes the performance of the V_2O_5/Zn cell with CSGE in comparison with reported ZIBs based on vanadium-based cathodes and aqueous electrolytes.

A systematic evaluation was conducted to compare the cycling durability and capacity retention of ZIB cells employing CSGE and AE (Figure 5h and Figures S20–S22). At 1.0 A g^{-1}, the Zn//V_2O_5 cell employing CSGE exhibited an initial specific discharge capacity of 254.2 mAh g^{-1}, whereas the cell with AE delivered 292.4 mAh g^{-1}. After 500 cycles, the CSGE-based cell retained a capacity of 120.3 mAh g^{-1}, while the AE-based cell exhibited a more pronounced decline to 106.4 mAh g^{-1}, underscoring the superior capacity retention enabled by CSGE. This enhanced durability is attributed to effective inhibition of electrochemical corrosion and suppression of dendritic Zn buildup at the anode [50]. In addition, mitigation of parasitic reactions at both electrode interfaces reduces surface passivation caused by insulating by-products, promoting more efficient interfacial charge transfer, consistent with the lower charge-transfer resistance (Figure 5e) [48].

3 | Conclusions

In conclusion, this work presents a sustainable electrolyte design based on a chia seed-derived hydrogel that replaces conventional water-based formulations for aqueous zinc-ion batteries. Prepared via a simple water extraction without synthetic additives, the chia seed gel electrolyte (CSGE) offers a scalable, low-cost, and environmentally benign platform. Its intrinsic hydrogen-bonded network and abundant hydrophilic and zincophilic functional groups effectively regulate Zn^{2+} solvation, suppress free-water activity, and stabilize the Zn/electrolyte interface, enabling homogeneous Zn deposition along the Zn(002) plane and long-term dendrite suppression. Consequently, the CSGE delivers a high Zn^{2+} transference number of 0.84, exceptional cycling stability exceeding 4000 h at 1.0 mA cm^{-2} and 1.0 mAh cm^{-2} in the Zn//Zn symmetric cells, and remarkable battery performance. The Zn//V_2O_5 cell utilizing CSGE delivers a specific discharge capacity of 338 mAh g^{-1} at 0.1 A g^{-1}. Beyond ZIBs, this green electrolyte strategy is readily extendable to other aqueous rechargeable batteries, offering a general pathway toward low-cost, safe, and sustainable energy storage technologies.

Conflicts of Interest

The authors declare no conflicts of interest.

Data Availability Statement

The data that support the findings of this study are available from the corresponding author upon reasonable request.

References

1. D. Deng, M. G. Kim, J. Y. Lee, and J. Cho, "Green Energy Storage Materials: Nanostructured TiO_2 and Sn-Based Anodes for Lithium-Ion Batteries," *Energy & Environmental Science* 2 (2009): 818–837, https://doi.org/10.1039/b823474d.

2. R. Yuksel, O. Buyukcakir, W. K. Seong, and R. S. Ruoff, "Metal-Organic Framework Integrated Anodes for Aqueous Zinc-Ion Batteries," *Advanced Energy Materials* 10 (2020): 1904215, https://doi.org/10.1002/aenm.201904215.

3. Z. Zhu, T. Jiang, M. Ali, et al., "Rechargeable Batteries for Grid Scale Energy Storage," *Chemical Reviews* 122 (2022): 16610–16751, https://doi.org/10.1021/acs.chemrev.2c00289.

4. O. Buyukcakir, J. Ryu, S. H. Joo, et al., "Lithium Accommodation in a Redox-Active Covalent Triazine Framework for High Areal Capacity and Fast-Charging Lithium-Ion Batteries," *Advanced Functional Materials* 30 (2020): 2003761, https://doi.org/10.1002/adfm.202003761.

5. C. Li, X. Xie, S. Liang, and J. Zhou, "Issues and Future Perspective on Zinc Metal Anode for Rechargeable Aqueous Zinc-ion Batteries," *Energy & Environmental Materials* 3 (2020): 146–159, https://doi.org/10.1002/eem2.12067.

6. S. Asadi Haris, S. Adhami, M. Abouali, S. Coskun, and R. Yuksel, "Mitigating Zinc Dendrite Formation and Parasitic Side Reactions in Aqueous Zn-Ion Batteries Via Laser-Assisted Carbonization of Cu-PANI Films on Zn Anodes," *Small* 21 (2025): 2410051.

7. A. Bayaguud, Y. Fu, and C. Zhu, "Interfacial Parasitic Reactions of Zinc Anodes in Zinc Ion Batteries: Underestimated Corrosion and Hydrogen Evolution Reactions and Their Suppression Strategies," *Journal of Energy Chemistry* 64 (2022): 246–262, https://doi.org/10.1016/j.jechem.2021.04.016.

8. S. Asadi Haris, S. Adhami, Z. Dasdelen Kepir, and R. Yuksel, *Advanced Materials Technologies* 11 01894, https://doi.org/10.1002/admt.202501894.

9. J. Hao, X. Li, S. Zhang, et al., "Designing Dendrite-Free Zinc Anodes for Advanced Aqueous Zinc Batteries," *Advanced Functional Materials* 30 (2020): 2001263, https://doi.org/10.1002/adfm.202001263.

10. S. A. Haris, S. Adhami, R. Yuksel, and S. O. Kim, "Bio-Inspired Zinc Anodes: Mitigating Dendrite Formation and Side Reactions in Aqueous Zinc Metal Batteries Using Laser Carbonized Chitosan Layer," *Small* 21 (2025): 2501293, https://doi.org/10.1002/smll.202501293.

11. W. Yang, Y. Yang, H. Yang, and H. Zhou, "Regulating Water Activity for Rechargeable Zinc-Ion Batteries: Progress and Perspective," *ACS Energy Letters* 7 (2022): 2515–2530, https://doi.org/10.1021/acsenergylett.2c01152.

12. C. Nie, G. Wang, D. Wang, et al., "Recent Progress on Zn Anodes for Advanced Aqueous Zinc-Ion Batteries," *Advanced Energy Materials* 13 (2023): 2300606, https://doi.org/10.1002/aenm.202300606.

13. M. Sun, K. Wan, Y. Huang, et al., "Playing With Water Molecules: "Repulsing" or "Trapping" to Exclude Water-Induced Side Reactions on Zn Metal Anode," *Advanced Functional Materials* 35 (2025): 2417890, https://doi.org/10.1002/adfm.202417890.

14. J. Zhang, Q. Wu, S. Yang, et al., "Bio-Inspired Hydroxyl-Rich Electrolyte Additive for Highly Reversible Aqueous Zn-Ion Batteries With Strong Coordination Chemistry," *Green Chemistry* 26 (2024): 6723–6734, https://doi.org/10.1039/D4GC01364F.

15. X. Xiao, F. Guo, H. Mi, et al., "Controlling Dendrite Growth With Xylan-Enhanced Hydroxyl-Rich Hydrogel Electrolyte for Efficient Zn-Ion Energy Storage," *ACS Sustainable Chemistry & Engineering* 12 (2024): 470–479, https://doi.org/10.1021/acssuschemeng.3c06287.

16. Q. Zhao, T. Xu, K. Liu, et al., "Biomass-Based Functional Materials for Rechargeable Zn-Ion Batteries," *Energy Storage Materials* 71 (2024): 103605, https://doi.org/10.1016/j.ensm.2024.103605.

17. W. Chen, S. Guo, L. Qin, et al., "Hydrogen Bond-Functionalized Massive Solvation Modules Stabilizing Bilateral Interfaces," *Advanced Functional Materials* 32 (2022): 2112609, https://doi.org/10.1002/adfm.202112609.

18. W. Guo, T. Hua, C. Qiao, Y. Zou, Y. Wang, and J. Sun, "Biomass-Based Electrolyte Design for Aqueous Zinc-Ion Batteries: Recent Advances and Future Outlook," *Energy Storage Materials* 66 (2024): 103244, https://doi.org/10.1016/j.ensm.2024.103244.

19. Y. Chen, F. Gong, W. Deng, H. Zhang, and X. Wang, "Dual-Function Electrolyte Additive Enabling Simultaneous Electrode Interface and Coordination Environment Regulation for Zinc-Ion Batteries," *Energy*

Storage Materials 58 (2023): 20–29, https://doi.org/10.1016/j.ensm.2023.03.010.

20. K. Zhao, G. Fan, J. Liu, et al., "Boosting the Kinetics and Stability of Zn Anodes in Aqueous Electrolytes With Supramolecular Cyclodextrin Additives," *Journal of the American Chemical Society* 144 (2022): 11129–11137, https://doi.org/10.1021/jacs.2c00551.

21. D. Geng, Y. Tang, X. Han, Z. Cheng, L. Han, and J. Liu, "Inhibition of Dendrite Growth and Side Reactions Using Histidine as Electrolyte Additive for Aqueous Zn-Ion Batteries," *International Journal of Electrochemical Science* 18 (2023): 100191, https://doi.org/10.1016/j.ijoes.2023.100191.

22. Y. Wang, T. Wang, P. Cui, et al., "Phosphated Electrolyte Enabling Dual Robust Electrode–Electrolyte Interfacial Reconstruction Toward Capable Zn Metal Batteries," *Advanced Functional Materials* 35 (2025): 2421363, https://doi.org/10.1002/adfm.202421363.

23. H. Zheng, Y. Huang, J. Xiao, et al., "Multi-Protection of Zinc Anode via Employing a Natural Additive in Aqueous Zinc Ion Batteries," *Chemical Engineering Journal* 468 (2023): 143834, https://doi.org/10.1016/j.cej.2023.143834.

24. Z. Zheng, S. Yan, Y. Zhang, et al., "An Ultrathin Natural Cellulose Based Hydrogel Membrane for the High-Performance Quasi-Solid-State Zinc-Ion Batteries," *Chemical Engineering Journal* 475 (2023): 146314, https://doi.org/10.1016/j.cej.2023.146314.

25. Z. Shen, Z. Zhai, Y. Liu, et al., "Hydrogel Electrolytes-Based Rechargeable Zinc-Ion Batteries Under Harsh Conditions," *Nano-Micro Letters* 17 (2025): 227, https://doi.org/10.1007/s40820-025-01727-y.

26. W. Chen, S. Guo, L. Qin, et al., "Hydrogen Bond-Functionalized Massive Solvation Modules Stabilizing Bilateral Interfaces," *Advanced Functional Materials* 32 (2022): 2112609, https://doi.org/10.1002/adfm.202112609.

27. R. Yuksel, "Aloe Vera-Based Green and Sustainable Electrolyte for Zinc Ion Batteries," *Advanced Sustainable Systems* 8 (2024): 2400396, https://doi.org/10.1002/adsu.202400396.

28. Y. B. Arikan, G. Komurcuoglu, S. Adhami, G. Yaman Uzunoglu, and R. Yuksel, "Flaxseed-Based Green Electrolyte Enabling High Electrochemical Stability for Advanced Zinc Ion Batteries," *Advanced Sustainable Systems* 10 (2026): 01707, https://doi.org/10.1002/adsu.202501707.

29. L. A. Muñoz, A. Cobos, O. Diaz, and J. M. Aguilera, "Chia Seeds: Microstructure, Mucilage Extraction and Hydration," *Journal of food Engineering* 108 (2012): 216–224.

30. E. Reyes-Caudillo, A. Tecante, and M. A. Valdivia-Lopez, "Dietary fibre content and antioxidant activity of phenolic compounds present in Mexican chia (Salvia hispanica L.) seeds," *Food Chemistry* 107 (2008): 656–663, https://doi.org/10.1016/j.foodchem.2007.08.062.

31. M. M. Tosif, A. Najda, A. Bains, et al., "A Comprehensive Review on Plant-Derived Mucilage: Characterization, Functional Properties, Applications, and Its Utilization for Nanocarrier Fabrication," *Polymers* 13 (2021): 1066, https://doi.org/10.3390/polym13071066.

32. Y. Wang, Z. Wang, W. K. Pang, et al., "Solvent Control of Water O—H Bonds for Highly Reversible Zinc Ion Batteries," *Nature Communications* 14 (2023): 2720, https://doi.org/10.1038/s41467-023-38384-x.

33. I. Kim, S. T. San, A. C. Mendhe, S. D. Dhas, S.-B. Jeon, and D. Kim, "Rheological and Electrochemical Properties of Biodegradable Chia Mucilage Gel Electrolyte Applied to Supercapacitor," *Batteries* 9 (2023): 512, https://doi.org/10.3390/batteries9100512.

34. K. Wu, J. Cui, J. Yi, et al., "Biodegradable Gel Electrolyte Suppressing Water-Induced Issues for Long-Life Zinc Metal Anodes," *ACS Applied Materials & Interfaces* 14 (2022): 34612–34619, https://doi.org/10.1021/acsami.2c05887.

35. J. Feng, J. Wang, Q. Gu, et al., "1 μm-Thick Robust Gel Polymer Electrolyte With Excellent Interfacial Stability for High-Performance Li Metal Batteries," *Advanced Functional Materials* 35 (2025): 2412287, https://doi.org/10.1002/adfm.202412287.

36. M. S. Rocha, L. C. Rocha, M. B. D. S. Feijó, P. L. L. D. S. Marotta, and S. C. Mourao, "Effect of pH on the Flaxseed (Linum Usitatissimum L. Seed) Mucilage Extraction Process," *Acta Scientiarum Technology* 43 (2021): 50457, https://doi.org/10.4025/actascitechnol.v43i1.50457.

37. C. Huang, X. Zhao, Y. Hao, et al., "Highly Reversible Zinc Metal Anodes Enabled by Protonated Melamine," *Journal of Materials Chemistry A* 10 (2022): 6636–6640, https://doi.org/10.1039/D1TA10517E.

38. L. Chen, "Stabilization of Zn Anodes via a Butanediol Additive," *Journal of Solid State Electrochemistry* 28 (2024): 507–515, https://doi.org/10.1007/s10008-023-05703-7.

39. L. Li, S. Jia, Z. Cheng, and C. Zhang, "Improved Strategies for Separators in Zinc-Ion Batteries," *Chemsuschem* 16 (2023): 202202330.

40. L. Zhao, Y. Li, M. Yu, Y. Peng, and F. Ran, "Electrolyte-Wettability Issues and Challenges of Electrode Materials in Electrochemical Energy Storage, Energy Conversion, and Beyond," *Advanced Science* 10 (2023): 2300283, https://doi.org/10.1002/advs.202300283.

41. Y. Wu, H. Wang, M. Xie, et al., "Superwetting Aqueous Electrolyte for Highly Stable Zinc Anodes," *Chemical Engineering Journal* 522 (2025): 168124, https://doi.org/10.1016/j.cej.2025.168124.

42. F. Yang, J. A. Yuwono, et al., "Understanding H_2 Evolution Electrochemistry to Minimize Solvated Water Impact on Zinc-Anode Performance," *Advanced Materials* 34 (2022): 2206754, https://doi.org/10.1002/adma.202206754.

43. A. Wu, S. Zhang, Q. Li, et al., "Multifunctional Crown Ether Additive Regulates Desolvation Process to Achieve Highly Reversible Zinc-Metal Batteries," *Advanced Energy Materials* 15 (2025): 2404450, https://doi.org/10.1002/aenm.202404450.

44. P. Boguta and Z. Sokołowska, "Zinc Binding to Fulvic Acids: Assessing the Impact of pH, Metal Concentrations and Chemical Properties of Fulvic Acids on the Mechanism and Stability of Formed Soluble Complexes," *Molecules* 25 (2020): 1297.

45. Q. Zhao, Z. Sun, H. Liu, H. Ying, and S. Dou, "A Systematic Understanding of Zinc Salts in Electrolyte Design for Aqueous Zinc-Ion Batteries," *ACS Nano* 19 (2025): 35237–35275, https://doi.org/10.1021/acsnano.5c10278.

46. Y. Zhu, J. Yin, X. Zheng, et al., "Concentrated Dual-Cation Electrolyte Strategy for Aqueous Zinc-Ion Batteries," *Energy & Environmental Science* 14 (2021): 4463–4473, https://doi.org/10.1039/D1EE01472B.

47. Y. Wang, Z. Wang, F. Yang, et al., "Electrolyte Engineering Enables High Performance Zinc-Ion Batteries," *Small* 18 (2022): 2107033.

48. C. Meng, W. He, L. Jiang, et al., "Ultra-Stable Aqueous Zinc Batteries Enabled by β-Cyclodextrin: Preferred Zinc Deposition and Suppressed Parasitic Reactions," *Advanced Functional Materials* 32 (2022): 2207732, https://doi.org/10.1002/adfm.202207732.

49. Y. Wang, L. Mo, X. Zhang, et al., "Regulating Water Activity for All-Climate Aqueous Zinc-Ion Batteries," *Advanced Energy Materials* 14 (2024): 2402041, https://doi.org/10.1002/aenm.202402041.

50. Z. Wang, J. Diao, J. N. Burrow, et al., "Urea-Modified Ternary Aqueous Electrolyte With Tuned Intermolecular Interactions and Confined Water Activity for High-Stability and High-Voltage Zinc-Ion Batteries," *Advanced Functional Materials* 33 (2023): 2304791, https://doi.org/10.1002/adfm.202304791.

51. Q. Meng, Q. Bai, R. Zhao, et al., "Attenuating Water Activity Through Impeded Proton Transfer Resulting From Hydrogen Bond Enhancement Effect for Fast and Ultra-Stable Zn Metal Anode," *Advanced Energy Materials* 13 (2023): 2302828, https://doi.org/10.1002/aenm.202302828.

52. B. Ren, X. Zhang, H. Wei, et al., "Suppressing Zinc Metal Corrosion by an Effective and Durable Corrosion Inhibitor for Stable Aqueous Zinc Batteries," *Advanced Functional Materials* 35 (2025): 2418594, https://doi.org/10.1002/adfm.202418594.

53. X. Zhang, L. Chen, R. Orenstein, et al., "Zincophilic and Hydrophobic Groups of Surfactant-Type Electrolyte Additive Enabled Stable Anode/Electrolyte Interface Toward Long-Lifespan Aqueous Zinc Ion

Batteries," *Energy Storage Materials* 70 (2024): 103500, https://doi.org/10.1016/j.ensm.2024.103500.

54. Z. Xiao, X. Dai, J. Zhu, et al., "Hydrogen Bond Competition Optimizing Aqueous Zn Ion Solvation and (002) Interfacial Deposition With Ultralong Stability," *Advanced Functional Materials* 35 (2025): 2424860, https://doi.org/10.1002/adfm.202424860.

55. Y. L. Chen, W. W. Yan, Y. F. Yuan, et al., "D-Lactitol Restructures Thick Inner Helmholtz Plane and Coordinates Multi-Zn^{2+} Solvation Sheath via Unique Adsorption Geometry and Super-Multi Zincophilic/Hydrophilic Sites," *Journal of Energy Storage* 133 (2025): 118102, https://doi.org/10.1016/j.est.2025.118102.

56. F. Bu, Y. Gao, W. Zhao, et al., "Bio-Inspired Trace Hydroxyl-Rich Electrolyte Additives for High-Rate and Stable Zn-Ion Batteries at Low Temperatures," *Angewandte Chemie International Edition* 63 (2024): 202318496, https://doi.org/10.1002/anie.202318496.

57. J. Shi, T. Sun, J. Bao, et al., ""Water-in-Deep Eutectic Solvent" Electrolytes for High-Performance Aqueous Zn-Ion Batteries," *Advanced Functional Materials* 31 (2021): 2102035, https://doi.org/10.1002/adfm.202102035.

58. H. Wang, M. Zhu, H. Wang, et al., "Rearrangement of H-Bonds Network of Solvation Structure via a Zincophilic Polyol-Type Surfactant to Stabilize Zinc Anode in Aqueous Zinc-Ion Batteries," *Energy Storage Materials* 67 (2024): 103238, https://doi.org/10.1016/j.ensm.2024.103238.

59. G. Duan, Y. Wang, B. Luo, et al., "Taurine-Mediated Dynamic Bridging Strategy for Highly Stable Zn Metal Anode," *Energy Storage Materials* 61 (2023): 102882.

60. J. Zhang, W. Huang, L. Li, et al., "Nonepitaxial Electrodeposition of (002)-Textured Zn Anode on Textureless Substrates for Dendrite-Free and Hydrogen Evolution-Suppressed Zn Batteries," *Advanced Materials* 35 (2023): 2300073, https://doi.org/10.1002/adma.202300073.

61. D. Yuan, J. Zhao, H. Ren, et al., "Anion Texturing Towards Dendrite-Free Zn Anode for Aqueous Rechargeable Batteries," *Angewandte Chemie* 133 (2021): 7289–7295, https://doi.org/10.1002/ange.202015488.

62. W. Chen, Z. Xie, H. Chen, and X. Wang, "Low-Cost Aqueous Electrolyte With MBA Additives for Uniform and Stable Zinc Deposition," *ACS Applied Materials & Interfaces* 16 (2024): 30580–30588, https://doi.org/10.1021/acsami.4c05430.

63. H. Liu, Z. Xin, B. Cao, et al., "Polyhydroxylated Organic Molecular Additives for Durable Aqueous Zinc Battery," *Advanced Functional Materials* 34 (2024): 2309840, https://doi.org/10.1002/adfm.202309840.

64. Y. Zhang, C. Peng, Z. Zeng, et al., "Sustainable Phytic Acid–Zinc Anticorrosion Interface for Highly Reversible Zinc Metal Anodes," *ACS Applied Materials & Interfaces* 14 (2022): 10419–10427, https://doi.org/10.1021/acsami.1c24288.

65. M. S. Javed, H. Lei, Z. Wang, B. Liu, X. Cai, and W. Mai, "2D V2O5 Nanosheets as a Binder-Free High-Energy Cathode for Ultrafast Aqueous and Flexible Zn-Ion Batteries," *Nano Energy* 70 (2020): 104573, https://doi.org/10.1016/j.nanoen.2020.104573.

66. Y. Zhang, Y. Huang, C. Zhang, et al., "Synergistic Solvation and Nucleation Regulation for Enhanced Stability and Longevity in Aqueous Zinc-Ion Batteries With d -Pantothenic Acid Additive," *ACS Sustainable Chemistry & Engineering* 13 (2025): 834–845, https://doi.org/10.1021/acssuschemeng.4c07186.

67. J. Hao, X. Li, X. Zeng, D. Li, J. Mao, and Z. Guo, "Deeply Understanding the Zn Anode Behaviour and Corresponding Improvement Strategies in Different Aqueous Zn-Based Batteries," *Energy & Environmental Science* 13 (2020): 3917–3949, https://doi.org/10.1039/D0EE02162H.

Supporting Information

Additional supporting information can be found online in the Supporting Information section.

Supporting File: adsu70510-sup-0001-SuppMat.docx.